PROCEEDINGS, 50th Workshop on Geothermal Reservoir Engineering
Stanford University, Stanford, California, February 10-12, 2025
SGP-TR-229

A Trust-region Based Sequential Implicit Nonlinear Solver for Geothermal Simulations

Sohail Waziri, Hamdi Tchelepi

Department of Energy Science & Engineering, Stanford University

swaziri@stanford.edu, tchelepi@stanford.edu

Keywords: geothermal, simulation, condensation problem, nonlinear solvers, trust region, coupling schemes, sequential methods

ABSTRACT

The so-called condensation problem poses numerical convergence challenges for nonlinear solvers. Herein, a single-cell condensation problem setup is used to demonstrate the conditional and restrictive nonlinear convergence of existing schemes, which include the fully coupled fully implicit method with standard Newton solver (*FIM*), the sequential fully implicit method (*SEQ*) with constant enthalpy during the Flow subproblem and constant total density during the Thermal subproblem and the modified sequentially preconditioned FIM (MSFIP-FIM). Then a new scheme, the trust-region based adaptive sequential fully implicit scheme (*aSEQ*), is proposed. *aSEQ* is composed of two parts; a trust-region relaxation based on prevention of crossing of kinks in the residual space for the Flow subproblem and adaptivity between constant pressure and constant total density constraint depending on phase conditions during the thermal subproblem. Using numerical examples, *aSEQ* is shown to have significantly superior nonlinear convergence compared to the mentioned existing methods in terms of the timestep size for which the convergence can be achieved and a larger convergence radius for a given timestep size. Modifications are proposed to generalize *aSEQ* to multiple cells and a one-dimensional example is used to demonstrate the significant computational savings of *aSEQ*.

1. INTRODUCTION

Geothermal energy is an attractive energy asset; It is renewable on a human timescale and has low carbon emissions. It involves the extraction of thermal energy from subsurface hot spots by the production of geofluid. Part of the extracted thermal energy is then converted into electricity through an electric generator. Because geothermal energy is available at all times of the day, it can act as a base load and thus provides a reliable alternative to other intermittent renewable energy sources. The decarbonization of electric grids has led to an increased volatility in net load and electricity market prices as variable renewable energy (*VRE*) sources take an increasing fraction of the grid (Denholm et al., 2015). Various mechanisms for flexible dispatch of geothermal energy have been proposed and its economic potential have been studied to allow geothermal plants to compete in *VRE* dominated grids (Aljubran & Horne, 2024; Ricks et al., 2022; Ricks et al., 2024).

In the management and development of geothermal fields, reservoir simulations play a vital role in ensuring sustainable extraction of energy from the subsurface rock and help in the forecast and optimization of production (O'Sullivan et al., 2001). A typical simulator for a conventional geothermal reservoir solves coupled mass and energy conservation equations describing two-phase (steam and water) flow and heat transfer in fractured porous media. The governing equations exhibit mixed parabolic-hyperbolic behavior; fluid flow and heat conduction are parabolic whereas the hyperbolic nature comes from the transport of mass and energy. Furthermore, a fluid model is embedded into the simulator to accurately describe the thermodynamic phase behavior of the geofluid (Faust & Mercer, 1977). The monolithic fully coupled fully implicit (*FIM*) method is the widely used solution strategy for geothermal simulations (Pruess et al., 1999). It constitutes solving the system of governing equations simultaneously. For a given timestep, Newton-Raphson is used to obtain a linear system which is solved, and the process is iterated over until convergence up to a tolerance is achieved. *FIM*, in most cases, benefits from unconditional stability and quadratic convergence close to the solution. On the other hand, sequential methods split the overall system of equations into smaller subproblems which are solved individually and sequentially in a particular order. If an outer loop is enforced, the scheme is termed iterative sequential. Otherwise, the scheme comes under the umbrella of explicit methods. The split of the overall system is naturally based on the physics that is being modelled. For instance, Poromechanics problems solved using sequential methods can be divided into a flow part and a geomechanics part. Similarly, geothermal systems can be separated into flow and thermal subproblems. The separation allows the utilization of specialized preconditioners and linear solvers that target the specific behavior of the individual physics. Also, the implementation of coupling existing single-physics, specialized simulators in a sequential framework is straight-forward and requires much less code development than using the same simulators in a fully coupled framework. This is especially pertinent to companies in the industry where mostly specialized simulators for particular physics already exist and so it is capital and time efficient to couple the existing simulators in a sequential setting. Furthermore, sequential methods employ a "divide and conquer" strategy where the complex multi-physics problems are deconstructed into smaller systems of single physics described by partial differential equations exhibiting a certain behavior. This deconstruction allows deeper understanding of the associated nonlinearities and provides insight into devising solution strategies that can capture them.

The condensation problem also referred to as the "negative compressibility" problem is a real subsurface phenomenon that is most pronounced in geothermal systems where cold water at constant pressure is injected into subsurface that exists at saturated conditions. Coats and Miller (1980) described the condensation problem using a single cell where the injection of cold water leads to the condensation of steam which then leads to a drastic reduction in the fluid's volume. Since the grid blocks are of constant volume, the cell pressure decreases resulting in further inflow of cold water and condensation of the steam. The cell pressure continues to decline until all the steam

condenses after which the pressure jumps to the injection pressure due to the small positive compressibility of liquid water and the inflow ceases. The effective compressibility of a two-phase water-steam system is significantly higher compared to the compressibility of either liquid water or steam alone (Grant & Sorey, 1979). Therefore, the phase transition from steam to liquid water results in a significant drop in steam phase volume which exceeds the expansion of the fluids. As a result, significant numerical convergence issues arise for the nonlinear solver when simulating the condensation problem.

The condensation problem has been discussed in Pruess et al. (1987) where the authors developed an analytical model for injection of cold water into a reservoir saturated with super-heated steam. The model assumed complete instantaneous thermodynamic equilibrium locally which entails a sharp front between liquid water and saturated steam. However, when validating their analytical model with numerical simulations, they observed a two-phase region separating the saturated vapor region from the cold injected water instead of a sharp front in the numerical simulations. They detected cyclic variations in pressure in the two-phase region which they characterized as entirely spurious and a result of the finite spatial discretization in the numerical simulations. The same phenomenon was observed in Falta et al. (1992) when simulating steam injection for underground water remediation. The pressure oscillations hindered the simulation performance. Blocking of backflow of cold water was proposed to prevent pressure oscillations in steam injection to improve nonlinear performance (Gudbjerg et al., 2004). However, the proposed method is not applicable to geothermal simulations where cold water is injected into the reservoir.

The fully coupled fully implicit method, *FIM*, owing to its unconditional stability, has been the go-to method used for the solution of nonlinear systems arising from multi-physics, multiphase flow in porous media. However, *FIM* has been shown to suffer from non-convergence when used for solving the condensation problem (Moncorgé & Tchelepi, 2018; Wang, 2015; Wong et al., 2018). Coupled compressibility, $c_{coupled}$, for the system of mass and energy balances and linear compressibility, c_{linear}, arising from the linearization of the coupled system using fully coupled, fully implicit discretization were defined in Moncorgé and Tchelepi (2018) where the authors attributed the convergence issue of *FIM* to the signs of $c_{coupled}$ and c_{linear}. It was proposed that whenever the two compressibilities share the same sign, which happens for very small timestep sizes, *FIM* is convergent. Wang (2015) argued that the signs of $c_{coupled}$ and c_{linear} being equal is not a sufficient condition for convergence and proposed a stricter restriction on timestep size based on preventing negative pressures from the first Newton iteration. Wong et al. (2018) analyzed the condensation problem in a sequential framework and put forward a sequential nonlinear solver that is convergent for larger timestep sizes than *FIM*. The sequential strategy involved solving the Flow subproblem for only two-phase cells followed by *FIM* applied to the whole domain. The Flow sub-solve served as a preconditioner to the *FIM* method by providing a better initial guess. Recently, a multi-level nonlinear solver based on continuous localization in physics was devised for the condensation problem (Wang & Voskov, 2022). The proposed solver operated in hierarchical parameter spaces where solution from the coarser level is fed as an initial guess to the next refined space. The methodology utilized the Operator-Based-Linearization approach to construct the multi-level physics parameterization (Voskov, 2017). The solver was shown to have superior nonlinear performance as compared to conventional Newton-Raphson based *FIM* in terms of fewer Newton iterations and lower CPU time.

In this work, the nonlinear performance of some existing nonlinear solvers and coupling schemes is studied using a single-cell condensation problem. Then, a trust-region based sequential solver, *aSEQ*, is proposed. The solver involves construction of a trust region for Flow subproblem based on phase state and application of a pressure relaxation if solution pathway tries to cross the boundaries of the trust region. In addition, *aSEQ* employs adaptivity in Thermal subproblem constraint, constant total density for two-phase state and constant pressure for single-phase conditions. *aSEQ* shows superior nonlinear performance compared to the existing nonlinear solvers for the single-cell setup. Next, the extension of the algorithm to multiple cells is discussed.

2. GOVERNING EQUATIONS

Non-isothermal, multiphase flow of a single component H_2O fluid in porous media is described by mass and energy conservation equations as given respectively:

$$\frac{\partial}{\partial t}\left(\phi \sum_{j=1}^{n_p} \rho_j S_j\right) + \nabla \cdot \left(\sum_{j=1}^{n_p} \rho_j \boldsymbol{u}_j\right) - \sum_{j=1}^{n_p} \rho_j \tilde{q}_j = 0 \tag{1}$$

$$\frac{\partial}{\partial t}\left((1-\phi)\rho_R U_R + \phi \sum_{j=1}^{n_p} \rho_j U_j S_j\right) + \nabla \cdot \left(\sum_{j=1}^{n_p} \rho_j h_j \boldsymbol{u}_j\right) + \nabla \cdot (\boldsymbol{K}\nabla T) - \sum_{j=1}^{n_p} \rho_j h_j \tilde{q}_j = 0 \tag{2}$$

Here, ϕ is the rock's porosity whereas U_R represents its internal energy. ρ_j, S_j, $\tilde{q}_j$, U_j and h_j denote the density, saturation, source/sink, internal energy and enthalpy of phase j, respectively. The combined thermal conductivity of the fluid and rock is given by $\boldsymbol{K}$ and T is the temperature. n_p refers to the total number of phases which are steam and liquid water, $j = \{s, w\}$. Fluid flow of each phase is modelled using the Darcy's law:

$$\boldsymbol{u}_j = -\boldsymbol{k}\frac{k_{rj}}{\mu_j}\left(\nabla p_j + \rho_j g \nabla z\right) \tag{3}$$

where $\boldsymbol{u}_j$, k_{rj}, μ_j and p_j refer to the Darcy velocity, relative permeability, viscosity, and pressure of phase j, respectively. g denotes the gravitational acceleration while depth is given by z. The thermodynamic phase behavior and fluid properties of the steam-water system are simulated using the model given in Faust and Mercer (1977). Molar formulation which involves using pressure and enthalpy as the primary variables is chosen as the nonlinear formulation. The choice is partially motivated by the fact that pressure and enthalpy remain independent of each other irrespective of the phase of the fluid and so variable switching is not required upon phase transitions. In addition to the conservation equations and the fluid model, the saturation constraint is enforced:

$$\sum_{j=1}^{n_p} S_j = 1 \tag{4}$$

Phase state of the fluid at a given pressure and enthalpy are determined using the saturation phase enthalpies as shown:

$$Fluid\ Phase\ State = \begin{cases} Two-phase,\ h_w(p) \le h \le h_s(p) \\ Liquid\ Water,\ h < h_w(p) \end{cases} \tag{5}$$

Finally, *CFL* is defined as:

$$CFL = \frac{q_{in}\Delta t}{V_p} \tag{6}$$

where q_{in}, Δt, and V_p are the total incoming volumetric flow rate, the timestep size and the pore volume of the injection cell, respectively.

3. SINGLE CELL CONDENSATION PROBLEM

3.1 Formulations

The condensation problem, sometimes referred to as the negative compressibility problem, can be appropriately described by injection of cold liquid water at constant pressure and enthalpy into a single cell that exists at saturated conditions as shown in Figure 1:

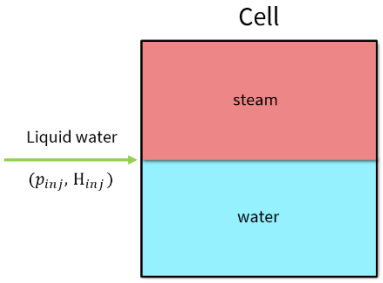

Figure 1: Setup for the single cell condensation problem.

The following assumptions are made:

1. Internal energy of the system equals its absolute enthalpy.
2. Energy contribution from rock is negligible.
3. Heat flow due to conduction is ignored.
4. Rock is incompressible.
5. Gravity and capillarity effects are ignored

The mass and energy balances for the cells are then given by:

$$V_p \frac{\partial \rho}{\partial t} = \Upsilon_{inj}(p_{inj} - p) \tag{7}$$

$$V_p \frac{\partial (\rho h)}{\partial t} = H_{inj}\Upsilon_{inj}(p_{inj} - p) \tag{8}$$

- $\rho = \sum_{j=1}^{n_p} S_j \rho_j$ where ρ is the total density of the fluid
- $\Upsilon_{inj} = \frac{kA}{\Delta x}\left(\frac{\rho}{\mu}\right)_{inj}$
- H_{inj} is the enthalpy of the injection fluid

Initial $\left(p_i = 10\ bar,\ \ h_i = 15732.832\frac{kJ}{kmole}\right)$ and boundary $\left(p_{inj} = 90\ bar,\ \ H_{inj} = 6175.919\frac{kJ}{kmole}\right)$ conditions are enforced. At the specified initial conditions, $S_w(p_i, h_i) = 0.1$ and $T(p_i, h_i) = 455\ K$, whereas the injected fluid is liquid water at a temperature of $355\ K$.

3.2 Apparent Compressibility, γ

Using chain rule and $\rho = \rho(p, h)$, the system of governing equations can be written as:

$$V_p \begin{bmatrix} \frac{\partial \rho}{\partial p} & \frac{\partial \rho}{\partial h} \\ h\frac{\partial \rho}{\partial p} & h\frac{\partial \rho}{\partial h} + \rho \end{bmatrix} \begin{bmatrix} \frac{\partial p}{\partial t} \\ \frac{\partial h}{\partial t} \end{bmatrix} = \begin{bmatrix} 1 \\ H_{inj} \end{bmatrix} \Upsilon_{inj}(p_{inj} - p) \tag{9}$$

Using Cramer's rule, the pressure equation can be derived as done in Wong et al. (2018):

$$\gamma \frac{\partial p}{\partial t} = \left(1 - \beta H_{inj}\right) \frac{\Upsilon_{inj}}{V_p} \left(p_{inj} - p\right) \tag{10}$$

where β and γ are defined as the following:

$$\beta = \frac{\frac{\partial \rho}{\partial h}}{h\frac{\partial \rho}{\partial h} + \rho} \tag{11}$$

$$\gamma = \frac{\partial \rho}{\partial p} - \beta \frac{\partial \rho}{\partial p} h \tag{12}$$

The absolute value of βH_{inj} for the parameter space of interest is such that $\left|\beta H_{inj}\right| < 1$. Thus, the term on the right side of Equation 10 is positive. Therefore, the direction of the change in pressure with time depends on the sign of γ. γ, termed as apparent compressibility, has contrasting signs depending on the phase of the fluid:

$$\gamma = \begin{cases} \gamma < 0, \ h_w(p) \le h \le h_s(p) \\ \gamma > 0, \ h < h_w(p) \end{cases} \tag{13}$$

h_w(p) and $h_s(p)$ are the enthalpy of saturated water and saturated steam respectively at the saturation pressure of p. So, the coupled condensation problem has a negative apparent compressibility, and pressure decreases as cold water is being injected into the cell up until all the steam has been condensed. This "anomalous" pressure response to injection is simulated and shown in Figure 2(a) where the negative apparent compressibility of water-steam mixture causes the cell pressure to drop from initial pressure of 10 bars until all the steam has undergone phase transition into liquid water. Also plotted in Figure 2(a) is the water saturation which increases linearly from 0.1 to 1. Beyond complete condensation, γ becomes positive and further injection leads to a sharp increase in pressure (as illustrated in Figures 2(a) and 2(b)) until the cell pressure equals the injection pressure of 90 bars and the inflow ceases. Another important observation is the proximity of the pressure-enthalpy evolution of the cell, shown in red in the zoomed-in plot in Figure 2(b), to the phase boundary, given in magenta colored dashed line. Nonlinear convergence issues, as will be discussed in later sections, are directly related to premature condensation. The physical solution, as a function of time, lying so close to the phase boundary contributes directly to the convergence issues associated with existing nonlinear solvers.

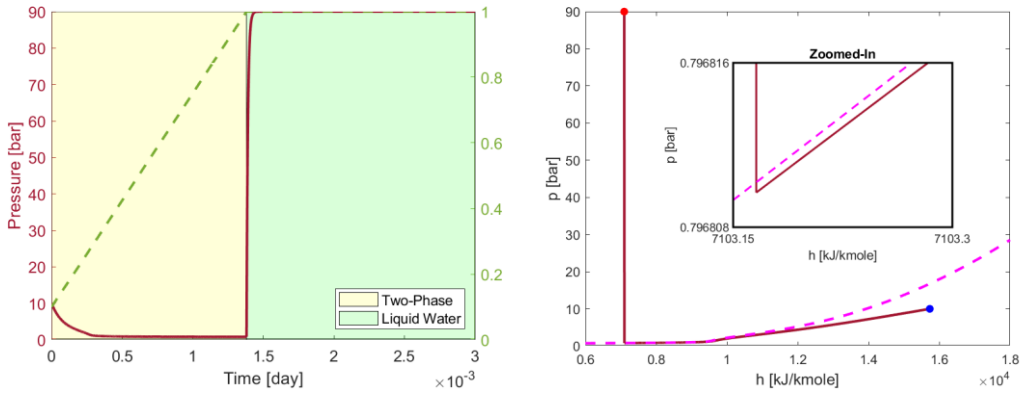

(a) (b)

Figure 2: (a) Plot of pressure (shown in red) and water saturation (shown in dashed green) for the single cell condensation problem as a function of time. (b) Pressure and enthalpy of the cell in a Phase diagram. The phase boundary between liquid water and two-phase region is shown in magenta colored dashed line. The blue and red dots indicate the solution at $t = 0\ days$ and $t = 0.003\ days$ ($CFL = 0.897$), respectively.

3.3 Existing Nonlinear Solution Strategies

Analyzing nonlinear convergence of existing nonlinear solvers is key to understanding why they exhibit poor convergence and to motivate the need to develop a more robust nonlinear solution strategy for the condensation problem. Subject to finite volume discretization in space and Backward Euler temporal discretization, we define the linearized mass and energy residuals:

$$R_M^{(n+1,k)} = V_p\left(\rho^{(n+1,k)} - \rho^{(n)}\right) - \Delta t \Upsilon_{inj}\left(p_{inj} - p^{(n+1,k)}\right) = 0 \tag{14}$$

$$R_E^{(n+1,k)} = V_p\left((\rho h)^{(n+1,k)} - (\rho h)^{(n)}\right) - \Delta t H_{inj} \Upsilon_{inj}\left(p_{inj} - p^{(n+1,k)}\right) = 0 \tag{15}$$

3.3.1 Fully Coupled, Fully Implicit Scheme

Herein, *FIM* refers to the fully coupled, fully implicit scheme that employs standard Newton-Raphson as its nonlinear solver. *FIM* solves the full system of the governing equations, given by Equation 16, for the primary variables, pressure and enthalpy:

$$\begin{bmatrix} \frac{\partial R_M}{\partial p} & \frac{\partial R_M}{\partial h} \\ \frac{\partial R_E}{\partial p} & \frac{\partial R_E}{\partial h} \end{bmatrix}^{(n+1,k)} \begin{bmatrix} p^{(n+1,k+1)} - p^{(n+1,k)} \\ h^{(n+1,k+1)} - h^{(n+1,k)} \end{bmatrix} = - \begin{bmatrix} R_M \\ R_E \end{bmatrix}^{(n+1,k)} \tag{16}$$

Here, $n+1$ and $k+1$ indicate the current time level and newton iteration, respectively. The process is iterated over until the norm of the residual drops below a specified tolerance. To explain the conditional convergence of *FIM* for the condensation problem, $c_{coupled}$, which is the compressibility associated with the coupled system and c_{linear}, which is derived from the pressure equation, subject to fully coupled fully implicit linearization, were derived in Moncorgé and Tchelepi (2018) :

$$c_{coupled} = \frac{\gamma}{\rho} \tag{17}$$

$$c_{linear} = c_{coupled} - \Delta t \frac{\xi}{\rho} \tag{18}$$

where $\xi = \left(\beta H_{inj} - 1\right) \frac{\Upsilon_{inj}}{V_p} < 0$ for two-phase region. The sign of $c_{coupled}$ equals the sign of γ which is negative for two-phase state whereas the sign of c_{linear} depends on the timestep size. For small Δt, both $c_{coupled}$ and c_{linear} are negative so the pressure is changed in the correct direction. However, for large Δt, c_{linear} becomes positive and Newton iteration would guide pressure in the wrong direction. We can derive a timestep size, $\Delta t_{sign\ change}$, above which the c_{linear} changes sign from negative to positive:

$$\Delta t_{sign\ change} := \frac{\gamma}{\xi} \tag{19}$$

It was shown, however, that $\Delta t < \Delta t_{sign\ change}$ is not a sufficient condition for convergence and a stricter criterion, Δt_{neg}, was derived based on preventing negative pressure from the first newton iteration (Wang, 2015):

$$\Delta t_{neg} := \frac{\gamma}{\xi} \frac{p}{p_{inj}} < \Delta t_{sign\ change} \tag{20}$$

To understand the effect of timestep size on the residual space and the convergence radius of *FIM*, we look at the residual contours given in Figure 3. From the contour plots, we observe that for timestep sizes when solution is in the two-phase region, sub-figures (a) to (c), the radius of convergence of *FIM* shrinks as the timestep size is increased; seven out of the 17 starting guesses, including using initial state as the initial guess, converge for sub-figure (a) whereas none of the initial guesses converge for (c). The other point to note is that using an initial guess that is in the single-phase liquid region for a timestep where the solution lies in the two-phase region is a poor choice for *FIM*. An interesting behavior is observed for $\Delta t = 2 \cdot 10^{-3}$ days (*CFL* = 0.8928) which is given in sub-figure (d) where neither the initial state as starting guess nor initial guesses that lie inside two-phase region converge to the solution. However, all the initial guesses that start in single-phase liquid region converge to the solution. So, if the solution lies in the single-phase region, *FIM* is convergent if we can provide a reasonable guess from the single-phase region.

Next, we approximate $(\Delta t_{conv})_{FIM}$ which is defined as the largest timestep size for which *FIM* is guaranteed to be convergent, through numerical simulations. Each simulation is a single timestep with timestep size starting from 10^{-6} days (*CFL* = 5.838*10^{-4}) until 2*10^{-3} days (*CFL* = 0.8928) with increments of 10^{-6} days. The results are summarized in Figure 4. Pressure from the first Newton iteration and the corresponding converged pressure are plotted in sub-figure (a). Sub-figure (b) plots the water saturation. Note that only results for timesteps for which *FIM* is convergent are shown. $(\Delta t_{conv})_{FIM}$ is found to be 6.7*10^{-5} days (*CFL* = 0.0413) which is less than Δt_{neg}. Another key takeaway is that for large timestep sizes when the solution resides in the single-phase region, *FIM* might be convergent even if the pressure and water saturation from the first Newton iteration is unphysical (see sub-figure (a) where $p^{k=1}$ is greater than p_{inj} =90 bars and $c_{coupled}$ and c_{linear} have opposing signs.

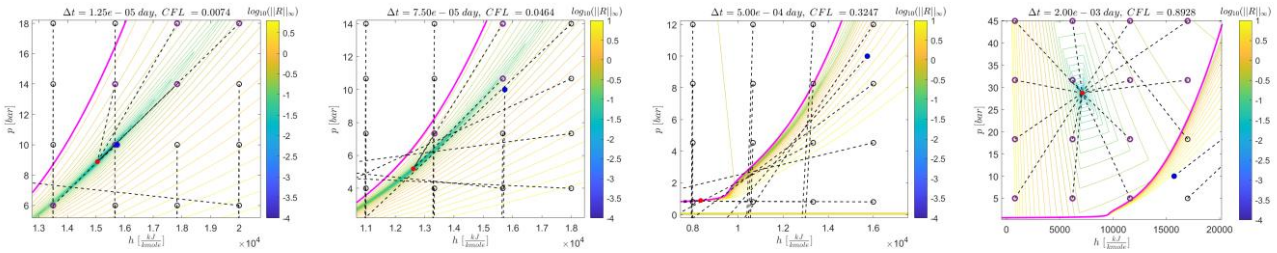

(a) 7/17 converged **(b) 3/17 converged** **(c) 0/17 converged** **(d) 14/17 converged**

Figure 3: Residual space and convergence characteristics of *FIM* for different timestep sizes and initial guesses. The contours are for increasing timestep size from left to right. The phase boundary is shown by solid magenta colored line. Blue and red dots show the initial state and converged solution, respectively. Black dashed line connects the initial guess with the

corresponding solution at the final Newton iteration after which either convergence or divergence is declared. Initial guesses which are displayed in purple edged dots converge to the solution whereas black edged dots diverge.

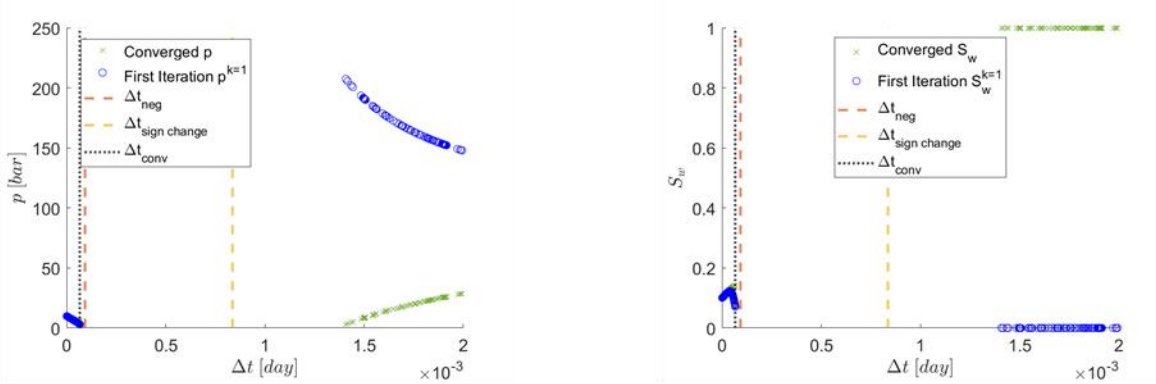

(a) **(b)**

Figure 4: Effect of timestep size on nonlinear convergence of *FIM*.

3.3.2 Sequential Fully Implicit Scheme

Sequential Fully Implicit schemes split the overall system into two subproblems, Flow subproblem and Thermal subproblem, corresponding to the mass and energy conservation equations, respectively. The subproblems are solved individually and an outer loop is used to iterate until the overall system converges. During individual sub-solves, a coupling parameter is fixed. Herein, *SEQ* refers to a sequential fully implicit scheme where the Flow subproblem is solved first at constant enthalpy, followed by the Thermal subproblem during which total density is kept constant, and the loop is iterated over until convergence up to some tolerance is achieved. An interesting characteristic of the *SEQ* scheme when applied to the condensation problem is that the first Newton iteration in the Flow subproblem always increases the pressure if solution from previous timestep is used as the initial guess:

$$p^{(n+1,v_F=1)} - p^{(n)} = \frac{\Delta t Y_{inj}\left(p_{inj} - p^{(n)}\right)}{V_p \frac{\partial \rho}{\partial p}\Big|_{\left(p^{(n)},\partial h=0\right)} + \Delta t Y_{inj}} \tag{21}$$

Figures 5 and 6 summarize the effect of timestep size on the nonlinear convergence of *SEQ*. There are three interesting observations to be made. Firstly, *SEQ* displays superior nonlinear convergence compared to *FIM* as *SEQ* converges for more starting points than *FIM* (compare sub-figures 5(a) and 5(b) to 6(a) and 6(b), respectively) and has larger Δt_{conv} ($(\Delta t_{conv})_{SEQ}$= 2.9*10^{-4} days > $(\Delta t_{conv})_{FIM}$ = 6.7*10^{-5} days). Secondly, the reason behind divergence for all divergent points is pressure becoming negative which is directly related to solution path erroneously going into the single-phase region when the converged solution is inside the two-phase region. This behavior is evident from sub-figures 5(a) to 5(c) and from sub-figure 6(b) where $S_w^{k=1}$ approaches 1 as timestep size approaches $(\Delta t_{conv})_{SEQ}$. Finally, when the solution is in the single-phase liquid region, see sub-figure 5(d), *SEQ* suffers from slow convergence further illustrated by sub-figures 6(c) and 6(d). Note that 20 sequential iterations is used as maximum sequential iterations and the simulation is terminated beyond 20 sequential iterations even though the residual norm was much higher than the desired tolerance which is set as 10^{-10}.

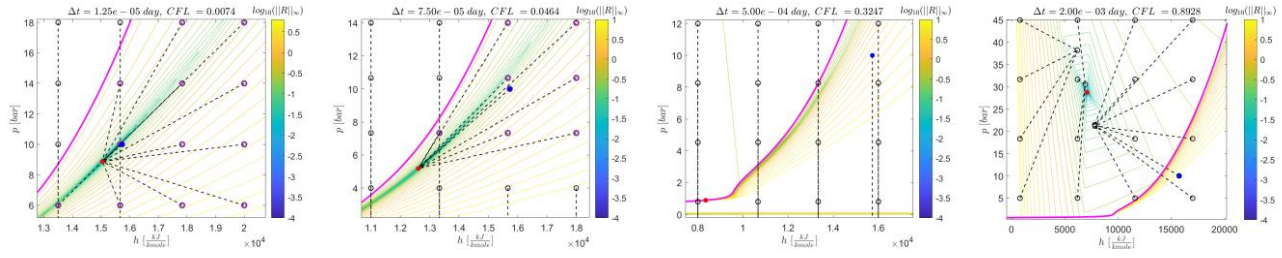

(a) 13/17 converged **(b) 8/17 converged** **(c) 0/17 converged** **(d) 0/17 converged**

Figure 5: Residual space and convergence characteristics of *SEQ* for different timestep sizes and initial guesses. The contours are for increasing timestep size from left to bottom. The phase boundary is shown by solid magenta colored line. Blue and red dots show the initial state and converged solution, respectively. Black dashed line connects the initial guess with the corresponding solution at the final Newton/sequential iteration after which either convergence or divergence is declared. Initial guesses which are displayed in purple edged dots converge to the solution whereas black edged dots diverge.

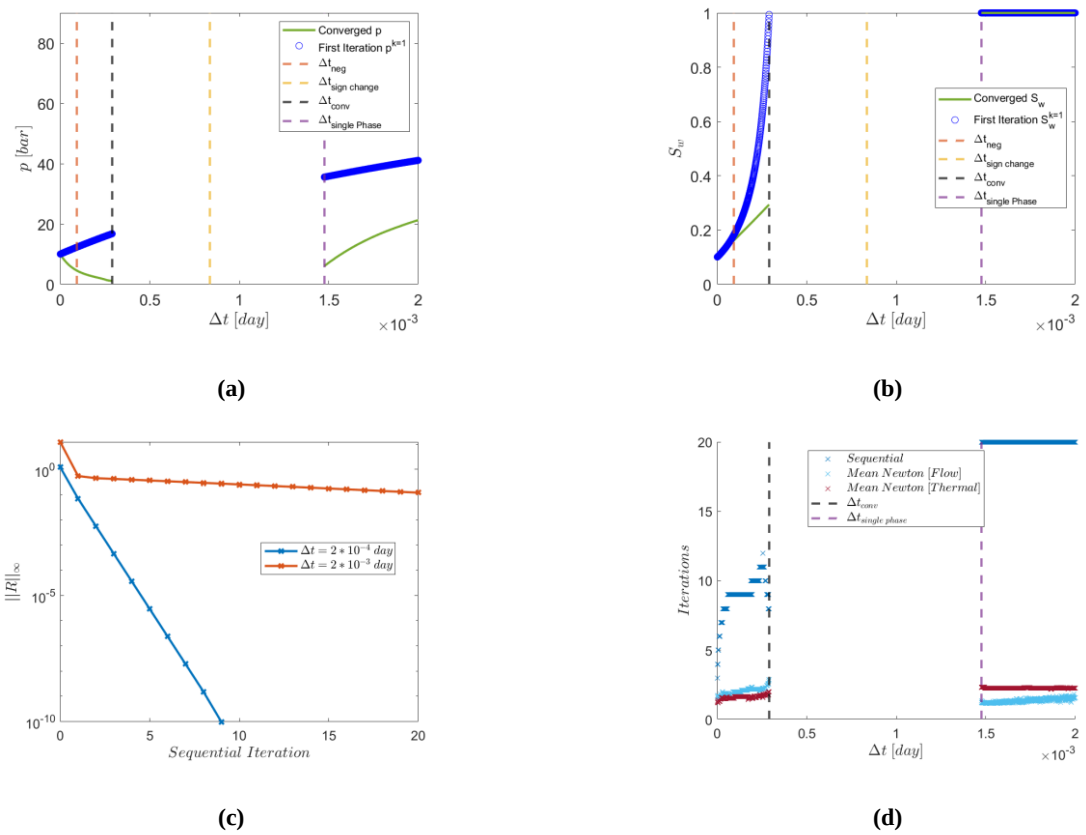

Figure 6: Effect of timestep size on nonlinear convergence of *SEQ*.

3.3.3 Preconditioned Fully Coupled Fully Implicit Scheme

A modified sequential fully implicit preconditioner was developed to improve nonlinear convergence of the *FIM* scheme for the condensation problem (Wong et al., 2018). The preconditioning step involved solving only the Flow subproblem and feeding the solution from the Flow subproblem as initial guess to *FIM*. Herein we would refer to this nonlinear strategy as *MSFIP-FIM*. The application of the preconditioner was adaptive i.e., it was only applied to cells at two-phase conditions.

MSFIP-FIM is applied to the single cell condensation problem and results are given in Figure 7 and 8. For timestep sizes where the solution lies inside the two-phase region, the preconditioning enlarges the convergence radius, as indicated by more starting guesses converging to the solution in sub-figures 7(a) and 7(b) as compared to *FIM*. Also, Δt_{conv} has also increased as a result of the preconditioning i.e., $(\Delta t_{conv})_{MSFIP-FIM}$ = 9.2*10^{-5} days > $(\Delta t_{conv})_{FIM}$ = 6.7*10^{-5} days, though the increase is not very significant. The main advantage of the preconditioner is that for large timestep sizes where phase transition has already occurred, and the solution is in the single-phase liquid region. The Flow subsolve in the preconditioning step takes the solution to the single-phase region where *FIM* is convergent given a reasonable initial guess. Sub-figure 7(d) and Figure 8 corroborates this behavior as *MSFIP-FIM* is convergent for all initial guesses irrespective of the phase status of the initial guess as long as the solution lies in the single-phase liquid region.

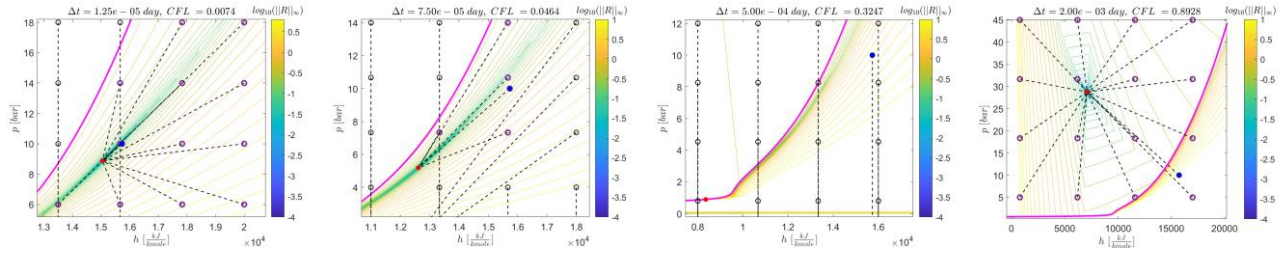

(a) 13/17 converged **(b) 5/17 converged** **(c) 0/17 converged** **(d) 17/17 converged**

Figure 7: Residual space and convergence characteristics of *MSFIP-FIM* for different timestep sizes and initial guesses. The contours are for increasing timestep size from left to right. The phase boundary is shown by solid magenta colored line. Blue and red dots show the initial state and converged solution, respectively. Black dashed line connects the initial guess with the corresponding solution at the final Newton/sequential iteration after which either convergence or divergence is

declared. Initial guesses which are displayed in purple edged dots converge to the solution whereas black edged dots diverge.

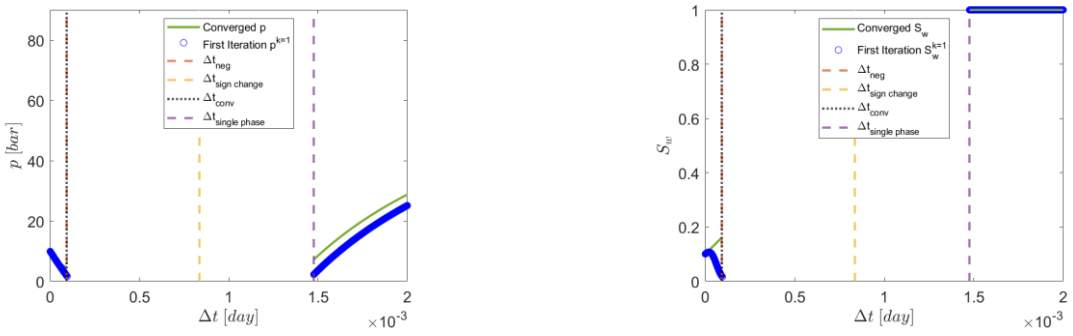

(a) **(b)**

Figure 8: Effect of timestep size on nonlinear convergence of *MSFIP-FIM*.

3.4 Trust-region based, Adaptive Sequential Fully Implicit Scheme

The existing nonlinear solvers fail to tackle the primary causes of non-convergence for the condensation problem, namely, negative pressures or in some rare cases negative enthalpies or negative densities. The underlying factor contributing to the solver pushing the solution towards unphysical regions is premature condensation. The early condensation leads to large changes in derivatives of density which in turn drive the primary unknowns towards negative values. The trust-region based adaptive sequential fully implicit solver (*aSEQ*) aims at keeping the solution path in a trust region where phase transition is only allowed if it is physical. Residual information at the phase boundary is used in guiding the solution path towards the true physical solution. The proposed nonlinear solver aims at overcoming three main shortcomings of the existing nonlinear solvers:

1. Divergence into non-physical region for intermediate timestep sizes where converged solution is in the two-phase region.
2. Conditional convergence contingent on the choice of the initial guess.
3. Slow sequential convergence as is the case for *SEQ* for large timestep sizes.

3.4.1 Components of *aSEQ*

aSEQ comprises of two essential components. Firstly, a correction is applied to the Newton update during the Flow subproblem to keep pressure in the trust region. Here, the trust region is defined for a given enthalpy, h, as the pressure interval between 0 and the saturation pressure at the given enthalpy, $p^{sat}(h)$, if the solution lies on the constant enthalpy line inside the two-phase region. On the other hand, if the solution is in the single-phase region, the trust region would then be the pressure interval between $p^{sat}(h)$ and injection pressure. Figure 9 plots R_M as a function p for a given h and helps visualizes the trust region and the kink in the residual at the phase boundary. The solution is of course not known a priori, but the sign of the mass residual at the saturation pressure ($R_M(p^{sat}(h), h)$) indicates the phase state of the solution. To explain how the sign of ($R_M(p^{sat}(h), h)$) is a marker of the solution's phase state, we look at the pressure update from the Flow Newton loop:

$$p^{(n+1,\nu_F)} = p^{(n)} - \frac{\mathrm{R_M}\left(p^{(n+1,\nu_F)},h^{(*)}\right)}{V_p\frac{\partial\rho}{\partial p}\Big|_{\left(p^{(n+1,\nu_F)},\partial h=0\right)}+\Delta t\Upsilon_{inj}} \tag{22}$$

where $h^{(*)}$is the enthalpy from previous sequential iteration. The denominator in the rightmost term is always positive. Therefore, the sign of mass residual affects whether pressure increases or decreases. A positive R_M would result would want to decrease the pressure and vice versa. From sub-figure 9(a), $R_M\left(p_{sat}(h^{(*)}, h^{(*)}\right)$ is positive and coincides with the kink in the residual. Solution (shown by green dot) lies below the saturation pressure and thus the two-phase region becomes the trust region. Note that updated pressure, if not relaxed, lies at the single-phase region (shown by red hollow dot numbered 1) and so the phase transition proposed by the Newton solver is not physical. If we take the pressure update without relaxation, the pressure becomes negative in the subsequent Newton iteration and thus erroneous phase transition leads to divergence. For the case where converged pressure in the Flow inner loop lies inside the single-phase region, the sign R_M would be negative implying that the trust region for pressure is above the saturation pressure i.e., the single-phase region as given in sub-figure 9 (b). Since the pressure update from the Newton solver (shown by red hollow dot numbered 1) also exists in the single-phase region, the condensation is physical and so no correction needs to be applied to the update.

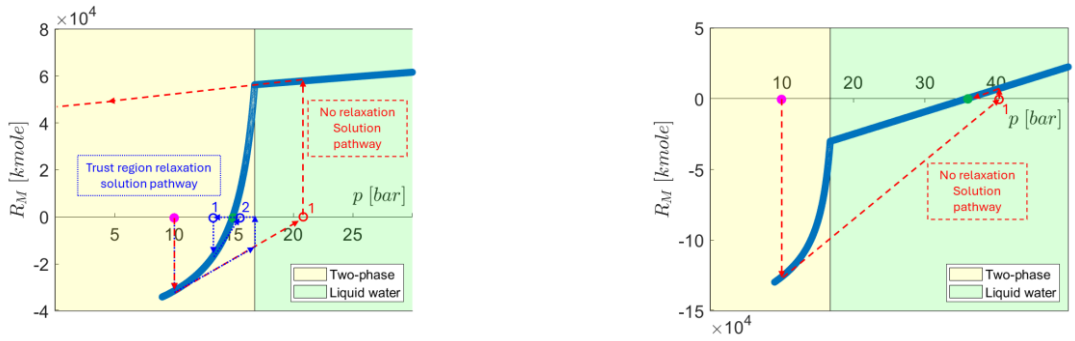

(a) converged pressure solution is inside two-phase region **(b) pressure solution is inside single-phase region**

Figure 9: Trust regions for the Flow subproblem. Pink solid dot is the initial guess whereas the green solid dot is the solution. The red dotted line is the Newton pathway without relaxation and blue dotted line shows the trust region relaxation pathway. Numbers next to the hollow dots indicate an iteration number.

Now that the mechanism for trust region selection has been established, the next step is to decide how to correct the update if Newton update is outside the trust region. The idea proposed is to simply take the midpoint of the pressure from previous iteration and the saturation pressure as shown by blue dotted line in sub-figure 9(a). Other corrections, based on minimizing the residual can be used as well. Algorithm 1 gives the trust-region correction of the Flow subproblem. The algorithm also includes relaxation of the pressure update when transitioning phase from single-phase liquid to two-phase region. This is added because trust region for the Thermal subproblem is not developed and for very restricted cases where the solution is in the two-phase region but very close to the saturation line, constant density lines, which are used as constraint for Thermal subproblem in the two-phase region, might intersect the saturation line causing erroneous condensation. In that scenario, the Flow trust-region solver would ensure relaxed entry back to the two-phase region in subsequent sequential iterations.

Algorithm 1: Trust Region for the Flow subproblem in a single cell setting

1: **if** $R_M(p^{sat}(h^v), h^v) > 0 \;\&\&\; p^{v_F} + \delta p^{v_F+1} > p^{sat}(h^v) \;\&\&\; S_w^{v_F} < 1$ **then**

2: $p^{v_F+1} = \dfrac{p^{sat}(h^v) + p^{v_F}}{2}$

3: **else if** $p^{v_F} + \delta p^{v_F+1} < p^{sat}(h^v) \;\&\&\; S_w^{v_F} > 1$ **then**

4: $p^{v_F+1} = p^{sat}(h^v) - \epsilon$

5: **else**

6: $p^{v_F+1} = p^{v_F} + \delta p^{v_F+1}$

7: **end if**

The other component of *aSEQ* is the adaptive switching between the coupling term that is kept constant during the Thermal subproblem:

$$Thermal\ Subproblem = \begin{cases} R_E(p(\partial\rho = 0), h) = 0, \;\; h_w(p) \le h \le h_s(p) \\ R_E(\partial p = 0, h) = 0, \;\; h < h_w(p) \end{cases} \tag{23}$$

The adaptivity is necessary because for Thermal subproblem, constant pressure inside two-phase region and constant density inside single-phase liquid region has shown to suffer from poor convergence or divergence (also illustrated by red line in sub-figure 6(c)) (Wong, 2018). The flow chart given in Figure 10 summarizes the *aSEQ* algorithm.

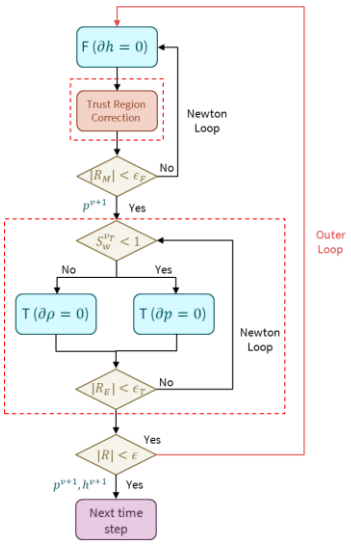

Figure 10: Flow chart of *aSEQ* algorithm. F and T refer to Flow and Thermal subproblems, respectively. The dashed boxes enclose the two components of aSEQ, namely, the trust-region correction and the adaptivity in thermal constraints depending on the phase state.

3.4.2 Nonlinear Performance of *aSEQ*

This section details the nonlinear performance of *aSEQ* for the single cell condensation problem. Figure 11 plots the residual space for various timestep sizes and initial guesses and we observe that *aSEQ* not only converges for larger timestep sizes but also has bigger convergence radius for a given timestep size as compared to existing nonlinear solvers. We also see that *aSEQ* is convergent irrespective of whether the initial guess is in the single-phase region or two-phase region. For instance, for sub-figures 11(a) to 11(c), the solution (shown by red dot) lies in the two-phase region and even when an initial guess that is in single-phase liquid region is used, *aSEQ* safely crosses the phase boundary and converges to the solution. Furthermore, *aSEQ*, due to the adaptivity in Thermal constraint, avoids the problem of slow sequential convergence that *SEQ* exhibits for large timestep sizes when all the steam has condensed (see subfigure 12 (c)). Also, irrespective of the timestep size, *aSEQ* is convergent and exhibits a good convergence rate as illustrated in sub-figure 12 (d)

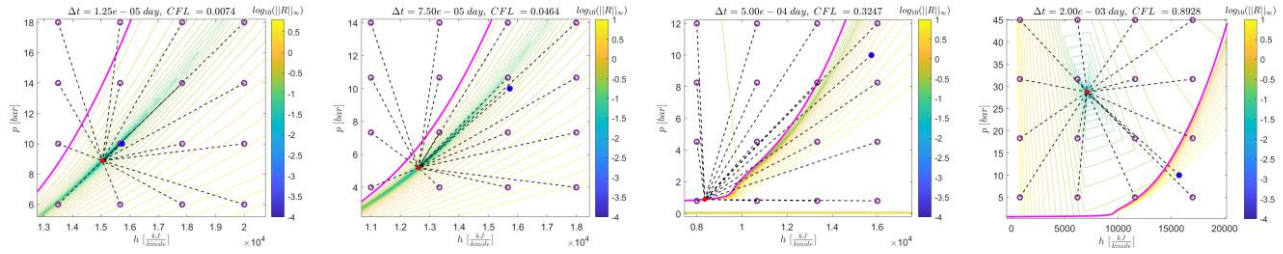

(a) 17/17 converged **(b) 17/17 converged** **(c) 17/17 converged** **(d) 17/17 converged**

Figure 11: Residual space and convergence characteristics of *aSEQ* for different timestep sizes and initial guesses. The contours are for increasing timestep size from left to right. The phase boundary is shown by solid magenta colored line. Blue and red dots show the initial state and converged solution, respectively. Black dashed line connects the initial guess with the corresponding solution at the final Sequential iteration after which either convergence is declared. Initial guesses which are displayed in purple edged dots converge to the solution whereas black edged dots diverge.

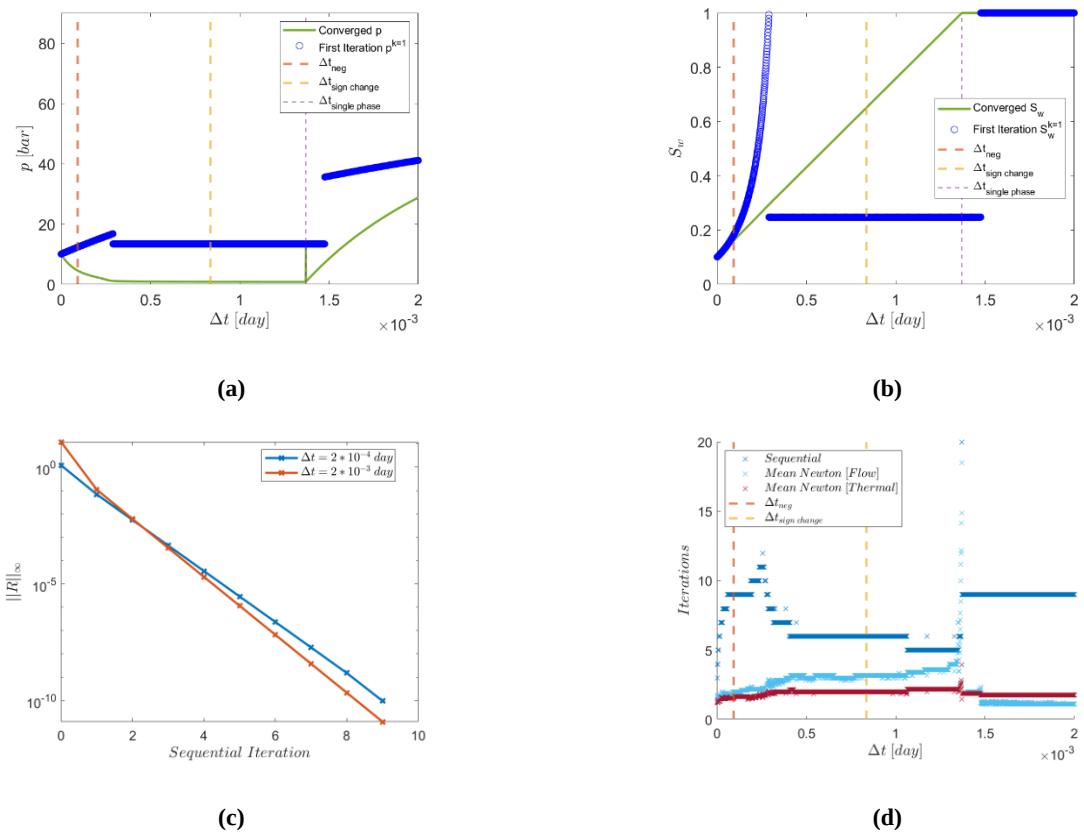

Figure 12: Effect of timestep size on nonlinear convergence of *aSEQ*.

3.4.3 Refinement Study of *aSEQ*

The physics of condensation problem requires that upon complete condensation, the cell pressure must increase instantaneously up to the injection pressure. However, as shown in sub-figures 12(a) and 12(b), the converged pressures are below the injection pressure (90 bars) for $S_w = 1$. To ensure that the difference is due to discretization error, a convergence study is carried out for solution at t_{sim} =2*10^{-3} days (*CFL* = 0.89). At time t_{sim}, p =28.75 bar and h = 7.1012*10^3 $\frac{kJ}{kmole}$. First, we simulate with $\Delta t = t_{sim}$ and then we cut the timestep size in half and simulate for two timesteps to get p and h at t. The process is repeated, and relative error is computed as:

$$\epsilon = \frac{Y - Y_{ref}}{Y_{ref}}, \quad Y = \{p, h\} \tag{24}$$

Note that the reference solution at the simulation time is computed using a very small timestep size and *FIM* as the nonlinear solver. Figure 13 plots the relative error as a function of timestep size. We observe that as the timestep size is decreased, the relative error decreases as well and the *aSEQ* solution approaches the reference solution.

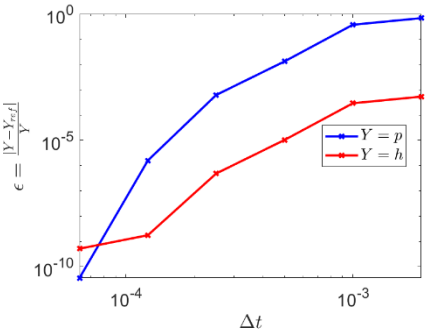

Figure 13: *aSEQ* refinement study.

4. EXTENSION OF ASEQ TO MULTIPLE CELLS

The previous section proposed *aSEQ*, a trust-region based sequential solver, for a single-cell condensation problem setup. This section deals with the extension of the algorithm to the condensation problem to multiple cells. The trust-region component of the algorithm is modified to enable the scaling; for a single cell, the sign of the mass residual at the phase boundary exactly determines the phase of the converged solution. However, for multiple cells, in addition to the sign of mass residual, flux derivatives and pressure increments of the neighboring cells also control the direction of pressure change:

$$\delta p_i = \frac{-R_{M_i} - \sum_{l=\{n_i\}} \frac{\partial R_{M_i}}{\partial p_l} \delta p_l}{\frac{\partial R_{M_i}}{\partial p_i}} \tag{25}$$

Here, $\{n_i\}$ is the set of neighboring cells of cell i and the sign of the summation term in the numerator is not necessarily an indicator of the phase of cell i if R_{M_i} were to be evaluated at the saturation pressure given the fixed enthalpy of cell. Nevertheless, we still know that the most significant kinks in the residual space still exist at the phase boundaries and thus, the trust region boundaries can be set a priori for a sequential iteration. This is because the discontinuities in the properties of H_2O across phase boundaries result in kinks in the residual space that are much more severe than kinks due to flow direction changes at cell interfaces. The pressure relaxation is applied whenever trust region boundaries are crossed irrespective of the phase of the converged solution (which cannot be known a priori). The modified trust-region relaxation algorithm for the Flow subproblem is given in Algorithm 2.

Algorithm 2: Trust Region for the Flow subproblem

if $p^{v_F} + \delta p^{v_F+1} > p^{sat}(h^v)$ && $S_w^{v_F} < 1$ **then**
  $p^{v_F+1} = p^{sat}(h^v) + \epsilon$
else if $p^{v_F} + \delta p^{v_F+1} < p^{sat}(h^v)$ && $S_w^{v_F} > 1$ **then**
  $p^{v_F+1} = p^{sat}(h^v) - \epsilon$
else if $p^{v_F} + \delta p^{v_F+1} < 0$ && $S_w^{v_F} < 1$ **then**
  $p^{v_F+1} = p^{sat}(h^v) - \epsilon$
else
  $p^{v_F+1} = p^{v_F} + \delta p^{v_F+1}$
end if

The adaptivity in Thermal constraint is general and thus applicable when scaling from a single cell to multiple cells. Hence, the same criterion as given in Equation 23 is used. Additionally, a physical check is added during Thermal loop that prevents enthalpy from becoming negative:

$$h^{v_T+1} = \begin{cases} \frac{h^{v_T}}{2}, & h^{v_T} + \delta h^{v_T+1} < 0 \\ h^{v_T} + \delta h^{v_T+1}, & else \end{cases} \tag{26}$$

4.1 1D Numerical Example

To test the performance of *aSEQ* for multiple cells' scenario, a one-dimensional condensation problem is set up, as given in Figure 14. The total number of cells is fixed at 50. Each cell has a pore volume of 40 m^3 with homogeneous geometric transmissibility of 5000 $\frac{cP \cdot m^3}{day \cdot bar}$ between cells. Uniform initial conditions $\left(p_i = 10\ bar,\ \ h_i = 15732.832 \frac{kJ}{kmole},\ S_{w_i} = 0.1\right)$ and linear relative permeabilities are used. Cold water at 90 bars and 6175.919 $\frac{kJ}{kmole}$ is injected into the leftmost cell. Initial timestep size is set at 10^{-7} days and the size of the timestep size is doubled upon success and halved upon failure until the total simulation time of 10^{-2} days. Tolerance for normalized residual norm is fixed as 10^{-5} for both inner loops and the sequential loop. A maximum of 20 iterations are allowed for inner loops and 200 iterations for sequential / newton loop (in case of *FIM*). Since the size of the system is small, direct linear solver is used.

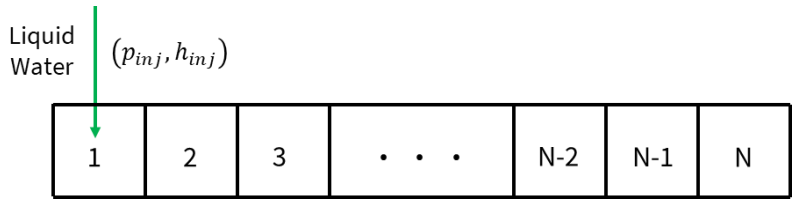

Figure 14: Setup for 1D condensation problem.

Three different nonlinear solution strategies are tested, namely, *FIM*, *MSFIP-FIM*, and *aSEQ*. Pressure, enthalpy and saturation fields at the end of simulation time are plotted in Figure 15. Table 1 summarizes the nonlinear performance of the three solvers. Since *FIM* and *MSFIP-FIM* have a similar timestep profile, the pressure, saturation and enthalpy fields match closely for the two compared to *aSEQ*. Nevertheless, there is a close match in the results. However, *aSEQ* outperforms both *FIM* and *MSFIP-FIM* in terms of computation cost since *FIM* and *MSFIP-FIM* require around two and a half times longer to complete the simulation. *aSEQ* takes only 22 timesteps and has just 5 timestep cuts. In contrast, *FIM* must perform 324 timesteps and cut 311 timesteps with similar numbers for *MSFIP-FIM*. Thus, *aSEQ* can take larger timestep size and save significant computational cost. Note that the overhead associated with computing saturation pressure for each cell per sequential iteration as required by the trust-region part of *aSEQ* is included in its runtime.

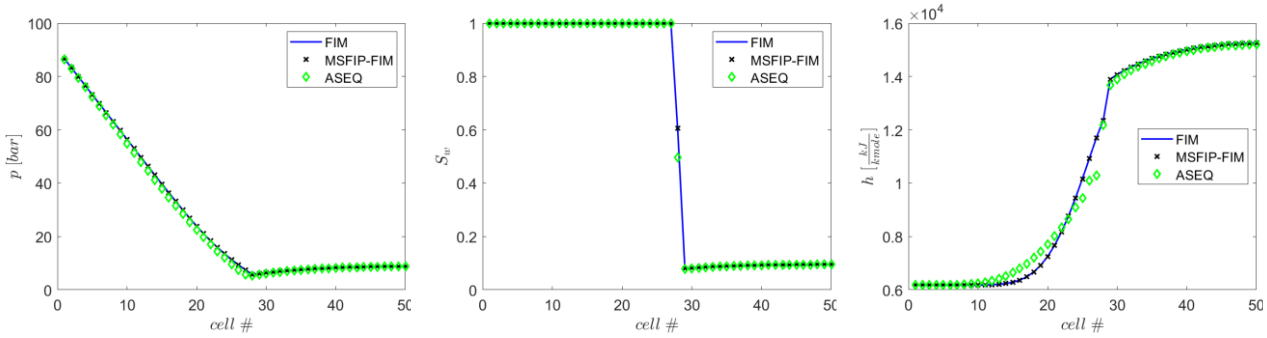

(a) **(b)** **(c)**

Figure 15: (a) Pressure, (b) Water saturation and (c) Enthalpy at the end of simulation time.

Table 1: Nonlinear performance of *FIM*, *MSFIP-FIM* and *aSEQ* for 1D condensation problem.

Solver	*FIM*	*MSFIP-FIM*	*aSEQ*
Normalized Runtime	2.50	2.76	1.00
Timesteps	324	314	22
Timestep Cuts	311	301	5
Sequential/Newton Iterations	17320	18039	2372
Maximum *CFL*	0.55	0.51	2.97

5. CONCLUSION

The Condensation problem poses a great challenge to nonlinear solvers. To motivate the development of robust solvers, existing nonlinear solution methods are studied using a single-cell setup of the condensation problem. The tested schemes include the fully coupled, fully implicit method with conventional Newton solver, *FIM*, the sequential fully implicit method, *SEQ*, and preconditioned *FIM* as proposed in Wong et al. (2018). All the tested schemes are shown to suffer from conditional and restrictive convergence, dependent on the choice of the timestep size. Then, a trust-region based nonlinear sequential strategy, *aSEQ*, is proposed. Severe kinks in the residual space are identified at the phase boundaries and a trust region is constructed accordingly for the Flow subproblem of *aSEQ*. During the Thermal sub-solve of *aSEQ*, adaptivity in the thermal constraint is employed at the Newton level. Extension of the algorithm to multiple cells is proposed. Using numerical examples, *aSEQ* is shown to have significantly improved nonlinear performance compared to the other solvers.

REFERENCES

Aljubran, J., and Horne, R. N.: FGEM: Flexible geothermal economics modeling tool, Applied Energy, 353, 122125 (2024).

Coats, K. H., and Miller, J. J. H.: Reservoir simulation: A general model formulation and associated physical/numerical sources of instability (1980).

Denholm, P., O'Connell, M., Brinkman, G., and Jorgenson, J.: Overgeneration from solar energy in California: A field guide to the duck chart, Technical Report, National Renewable Energy Laboratory (NREL), Golden, CO (United States) (2015).

Falta, R. W., Pruess, K., Javandel, I., and Witherspoon, P. A.: Numerical modeling of steam injection for the removal of nonaqueous phase liquids from the subsurface: 2. Code validation and application, Water Resources Research, 28(2), 451–465 (1992).

Faust, C. R., and Mercer, J. W.: Finite-difference model of two-dimensional, single-, and two-phase heat transport in a porous medium: Version I, 77, Department of the Interior, Geological Survey (1977).

Grant, M. A., and Sorey, M. L.: The compressibility and hydraulic diffusivity of a water-steam flow, Water Resources Research, 15(3), 684–686 (1979).

Gudbjerg, J., Trötschler, O., Färber, A., Sonnenborg, T. O., and Høgh Jensen, K.: On spurious water flow during numerical simulation of steam injection into water-saturated soil, Journal of Contaminant Hydrology, 75(3-4), 297–318 (2004).

Moncorgé, A., and Tchelepi, H. A.: Negative compressibilities for steam/water flow in porous media (2018).

O'Sullivan, M. J., Pruess, K., and Lippmann, M. J.: State of the art of geothermal reservoir simulation, Geothermics, 30(4), 395–429 (2001).

Pruess, K., Calore, C., Celati, R., and Wu, Y. S.: An analytical solution for heat transfer at a boiling front moving through a porous medium, International Journal of Heat and Mass Transfer, 30(12), 2595–2602 (1987).

Pruess, K., Oldenburg, C. M., and Moridis, G. J.: TOUGH2 User's Guide Version 2, Lawrence Berkeley National Laboratory Report LBNL-43134 (1999).

Ricks, W., Norbeck, J., and Jenkins, J.: The value of in-reservoir energy storage for flexible dispatch of geothermal power, Applied Energy, 313, 118807 (2022).

Ricks, W., Voller, K., Galban, G., Norbeck, J. H., and Jenkins, J. D.: The role of flexible geothermal power in decarbonized electricity systems, Nature Energy, (2024), 1–13.

Voskov, D. V.: Operator-based linearization approach for modeling of multiphase multi-component flow in porous media, Journal of Computational Physics, 337, 275–288 (2017).

Wang, Y.: A stability criterion for the negative compressibility problem in geothermal simulation and discrete modeling of failure in oil shale pyrolysis process, Master's Thesis, Stanford University (2015).

Wang, Y., and Voskov, D.: High-enthalpy geothermal simulation with continuous localization in physics, Mathematics, 10(22), 4328 (2022).

Wong, Z. Y.: Sequential-implicit Newton's method for geothermal reservoir simulation, Stanford University (2018).

Wong, Z. Y., Horne, R. N., and Tchelepi, H. A.: Sequential implicit nonlinear solver for geothermal simulation, Journal of Computational Physics, 368, 236–253 (2018).